ACS APPLIED MATERIALS & INTERFACES

Energy, Environmental, and Catalysis Applications

Paper-Derived Flexible 3D Interconnected Carbon Microfiber Networks with Controllable Pore Sizes for Supercapacitors

Pengcheng Dai, Yanming Xue, Shuo Zhang, Lei Cao, Daiming Tang, Xin Gu, Liangjun Li, Xuebin Wang, Xiangfen Jiang, Dandan Liu, Lingzhao Kong, Yoshio Bando, Dmitri V. Golberg, and Xuebo Zhao

ACS Appl. Mater. Interfaces, **Just Accepted Manuscript** • DOI: 10.1021/acsami.8b13281 • Publication Date (Web): 08 Oct 2018

Just Accepted

ACS Publications

is published by the American Chemical Society. 1155 Sixteenth Street N.W., Washington, DC 20036

Paper-Derived Flexible 3D Interconnected Carbon Microfiber Networks with Controllable Pore Sizes for Supercapacitors

Pengcheng Dai[†], Yanming Xue[‡,§], Shuo Zhang[†], Lei Cao[†], Daiming Tang[‡], Xin Gu[†], Liangjun Li[†], Xuebin Wang[‡,‖]*, Xiangfen Jiang[‡], Dandan Liu [†], Lingzhao Kong[⊥], Yoshio Bando[‡], Dmitri Golberg[‡,#], Xuebo Zhao[†]**

† State Key Laboratory of Heavy Oil Processing, Institute of New Energy, China University of Petroleum (East China), Qingdao 266580, P. R. China

‡International Center for Materials Nanoarchitectonics (WPI-MANA), National Institute for Materials Science (NIMS) Namiki 1-1, Tsukuba, Ibaraki, 305-0044, Japan.

§School of Materials Science and Engineering, Hebei University of Technology, Tianjin, 300130, P. R. China.

‖National Laboratory of Solid State Microstructures, Collaborative Innovation Center of Advanced Microstructures, College of Engineering and Applied Sciences, Nanjing University, Nanjing 210093, P. R. China.

⊥Shanghai Advanced Research Institute, Chinese Academy of Sciences, Shanghai, 201210, P. R. China

#School of Chemistry, Physics and Mechanical Engineering, Science and Engineering Faculty, Queensland University of Technology (QUT), 2nd George St., Brisbane, QLD 4000, Australia

*E-mail: zhaoxuebo@upc.edu.cn; ym.xue@hebut.edu.cn; wangxb@nju.edu.cn

KEYWORDS: cellulose paper · heteroatom-doping · carbon microfiber networks · controllable pore sizes · flexible supercapacitor

ABSTRACT: Heteroatom-doped three dimensional (3D) carbon fiber networks have attracted immense interest because of their extensive applications in energy storage devices. However, their practical production and usage remain a great challenge due to the costly and complex synthetic procedures. In this work, flexible B, N, and O heteroatom-doped 3D interconnected carbon microfiber networks (BNOCs) with controllable pore sizes and elemental contents were successfully synthesized via a facile one-step "chemical vapor etching & doping" (CVE&D) method by using cellulose-made paper, the most abundant and cost-effective biomass, as original network-frame precursor. Under a rational design, the BNOCs exhibited interconnected microfiber-network structure as expressways for electron transport, spacious accessible surface area for charge accumulation, abundant mesopores and macropores for rapid inner-pore ion diffusion, and lots of functional group for additional pseucapacitance. Being applied as binder-free electrodes for supercapacitors, BNOC-based supercapacitors not only revealed a high specific capacitance of 357 F g^{-1}, a high capacitance retention of 150 F g^{-1} at 200 A g^{-1}, a high energy density of 12.4 Wh kg^{-1} and a maximum power density of 300.6 kW kg^{-1} with aqueous electrolyte in two electrode configuration, but also exhibited a high specific capacitance of up to 242.4 F g^{-1} in all solid state supercapacitor.

Developing low-cost and high-performance energy storage systems (EESs) has become a crucial factor to meet the growing needs of new-generation electronics.[1-3] Among promissing technologies such as batteries, fuel cells and supercapacitors[2, 4, 5], electrochemical double layer supercapacitors (EDLSs), where capacitance comes from pure electrostatic charge accumulation

at the interface of electrode (such as carbon-based material) and electrolyte, have drawn prime attentions due to their high power density, long cycle lifetime and fast charge/discharge rates. [6-8] To date, activated carbons (ACs) have principally been used as electrode materials for industrial supercapacitors due to their high surface area, good stability and low-cost preparation.[9, 10] However, the structural shortcomings, such as powder morphology, non-beneficial pore size distribution, and limited surface functionalization make ACs suffer from limited energy density, low conductivity and slow inner pore ion diffusion.[4, 9] Especially, AC based supercapacitors need insulated polymer binders, such as polytetrafluoroethylene (PTFE) and polyvinylidenefluoride (PVDF). The additive insulated binders introduce extra cost, needless weight, and high contact resistance, which are not compatible with next-generation electronic devices such as roll-up displays, hand-held devices, and wearable multi-media.[11-13]

Enormous efforts have therefore been spent on developing novel porous carbon architectures with more benificial pore structures and surface functionalizations. Recently, 3D interconnected carbon architectures, such as 3D graphene membranes, 3D carbon nanotubes and 3D carbon fiber networks, are believed to be promising supercapacitor candidates due to their binder-free processing and excellent conductivity.[14-34] Especially, heteroatom (such as B, N, O, P and S) doping in 3D porous carbon architectures[22-27], which provides extra pseudocapacitance and significantly enhances the energy density, has been the focus of research. Comparing with other carbon materials, hierarchical porous carbon fiber networks have many advantages: (i) the 1D fiber network feature is beneficial for fast electron transport[35, 36]; (ii) the extremely high length-to diameter ratio and hierarchical porous structure provides a reduced ion diffusion pathway and high contact area between the active sites and the electrolyte[37, 38]; (iii) the overall hollow network structure guarantees fast ionic transport in electrolyte[39]. Therefore, various strategies have been

developed to make hierarchical porous carbon fiber networks[3, 13, 23, 32, 35, 36, 39-45]. For instance, Zhang group synthesized meso-macroporous carbon fiber network by electrospinning of polymer/SiO_2 blended solution, followed by pyrolysis and SiO_2 removal processes[42]; Lou group developed an electrospinning and carbonization method to prepare hollow particle-based N-doped carbon nanofibers using ZIF-8 as template to form hierarchical porous structures[43]. Song et. al, reported that high-surface-area carbon nanofiber films can be obtained by KOH-coating and heat treatment of electrospun phenolic-based nanofiber paper[41]. However, the current prevailing strategies, including template-directed synthesis and polymer-derived fabication, need costly ingredients or complex synthetic procedures as well as additional doping or active processes, which are unfavourable for scalable production[46, 47]. A one-step and cost-effective synthesis without additional activation process and costly ingredients toward obtaining 3D carbon fiber networks is highly imperative for the compact design of new energy storage devices.

Paper, one of the most ancient flexible products, is a promising precursor due to their wide availability, low cost, light weight, recyclability, and bendability. Especially, its network-frame morphology is quite suitable as a precursor for the preparation of carbon fiber networks. However, the state-of-art porous carbon materials obtained using paper as precursor are either non-flexible[48] or suffering from limited energy density[49], which limited their practical usage. In the present work, a series of flexible B, N, O co-doped 3D nanoporous carbon microfiber networks (BNOCs) with controllable pore sizes were successfully synthesized via a facile one-step "chemical vapor etching & doping" (CVE&D) method by using cellulose-made paper, the most abundant and cost-effective biomass, as the original network-frame precursor. After such CVE&D process, not only the interconnected microfiber network structure was well maintained within the as-synthesized BNOCs, but also hierarchical porous structures within their fiber units

were controllably created. The regarded unique network architectures could enable a spatially continuous convenience toward high-efficient electron transport, whereas the hierarchical porous structures endowed high surface area and rapid inner-pore ion transport. Serving as binder-free flexible electrodes, BNOCs demonstrated good performances in EDLSs with aqueous electrolyte (specific capacitance of 357 F g^{-1} at 0.1 A g^{-1} and 150 F g^{-1} at 200 A g^{-1}, energy density of up to 12.4 Wh kg^{-1} and maximum power density of 300.6 kW kg^{-1}), as well as in all solid state supercapacitor (specific capacitance of 242.4 F g^{-1} at 1 A g^{-1}).

Results and discussion

Synthesis and characterization of BNOCs.

The general CVE&D strategy for fabricating BNOCs is illustrated in Figure 1. In the process, filter papers (99% α-cellulose) were carbonized when the temperature went to 1000 ℃, resulting in solid carbon microfibers with a smooth surface (Figure S1). Meanwhile, vaporised boric acid carried by the flowing ammonia gas reacted with the obtained carbon microfibers[44, 49], generating abundant nano-pores and resulting in *in-situ* B, N, and O doping. In this way, BNOCs with different specific surface areas, pore size distributions and elemental contents were fabricated by adjusting the CVE&D time from 10 min, 20 min, 30 min to 40 min (denoted as BNOC-10, BNOC-20, BNOC-30 and BNOC-40, respectively.).

The BNOCs exhibited flexibility as good as the original paper precursor (Figure 2a, Movie S1). The typical scanning electron microscope (SEM) images of BNOC-30 revealed a membrane morphology (thickness of ~ 40 μm, as shown in Figure 2b) consisting of intertwined microfibers (Figure 2c). These intertwined microfibers

interconnected with their branches, and formed a continuous network, as depicted in Figure 2d. The fiber units of BNOCs possessed a rough surface (different from that of the original carbonized fiber with smooth surfaces, seen in Figure S1), and had a lot of pores consisting of multilayered ultrathin walls inside their bodies (Figure 2e-f, the magnified SEM and TEM features). More interestingly, the ultrathin BNOC films (thickness of ~ 10 nm, as shown in Figure 2g and h) were obtained when the sample experienced strong ultrasonic exfoliation. An average distance between randomly oriented graphitic planes (Figure 2h) was detected as ~ 0.345 nm from the films' folded parts; some turbostratic graphitic layers were clearly observed from the in-plane images. Domain boundaries and holes were seen between the lattices, which might be caused by a loss of volatile species or etching of amorphous carbon by ammonia gas or boric acid.[20] It is considered that an additional increase in surface area could be resulted from these abundant edges and holey structures. Moreover, two Raman peaks located at ~1590 cm^{-1} (G band) and ~2800 cm^{-1} (2D band) in BNOC-30 sample's Raman spectrum (Figure 2i) indicated that these few-layered graphitic structures have some extent of graphitization, while the D band (1340 cm^{-1}) indicated the presence of some turbostratic motifs and numerous defects, such as edges and holes.[20, 23]

Elemental contents and species distribution of BNOCs were studied by Electron energy loss spectroscopy (EELS) and X-ray photoelectron spectroscopy (XPS), as shown in Figure 3. The EEL spectra revealed that B, N, O atoms were effectively incorporated and nearly homogeneously distributed throughout the microfibers (Figure 3a-e). B and N contents at the microfiber edge were higher than those in its center, demonstrating a peculiar outside-in doping process during the CVE&D reaction. XPS data provided the specific contents of the elements

(Figure S2, Figure 3f) and also confirmed the detailed chemical states of both host- (C) and hetero- (B, N and O) elements on the topmost surfaces (Figure 3g-j).[50] For the samples without any doping, no B and N traces could be detected, only a small O content (~2.4 at.%) appeared. Along with the increase of doping time, the contents of doping elements all progressively increased, and maximized at BNOC-40, for which atomic fractions were 8.8 %, 9.7 % and 9.7 % for B, N, and O, respectively. The amount of protons were detected by elemental analyser, and the ratios of protons in weight were 2.78 wt%, 2.99 wt%, 3.55 wt% and 3.86 wt% for BNOC-10, BNOC-20, BNOC-30 and BNOC-40, respectively. The asymmetric C 1s peak of BNOC-30 could be fitted into four peaks (at 284.6 eV, 285.2 eV, 286.1 eV, and 289.6 eV), corresponding to the chemical environment of carbon atoms bonded to C, B, N and O[11]. Two peaks (at 191 eV and 192.3 eV) of B 1s spectrum suggested that certain amounts of boron atoms were directly bonded to carbon or nitrogen atoms in the form of B-C and B-N configurations, and with oxygen in the form of B-OH bonding [11]. The N 1s could be fitted as pyridinic N (398.1 eV), pyrrolic N (400.1 eV), graphitic N (401.3 eV) and C-N-B species (399.2 eV)[11]. Two peaks of O 1s spectrum were identified as OH and adsorbed water and/or oxygen (Figure 3j)[51]. The existence of C-N, C-B, C-O bonds is a solid evidence that the doped N, B, O atoms were bonded to the carbon lattice rather than physically adhered to the surface. Moreover, a large amount of functional groups (generated by B, N and O doping) were distributed on the outermost surface of BNOC, which are extraordinarily active and provide additional high pseudocapacitance. [52, 53]

Furthermore, we achieved an adaptive pore size distribution by utilizing the controllable CVE&D process. As illustrated in Figure 4a, BNOCs fabricated over various CVE&D times exhibited clearly distinguishing nitrogen adsorption/desorption isotherms. For instance, BNOC-10 exhibited type I isotherm. And the steep region at very low

relative pressure (less than 0.05) indicated filling of very narrow micropores, while limiting uptake was dependent on the accessible micropore volume. Correspondingly, there was a major microporous fraction (1.35 nm) and a puny amount of mesopores (2.3 nm) in BNOC-10 (Figure 4b). BNOC-20 had type I isotherm as well, but showed a secondary uptake at about P/P_0=0.01 and P/P_0=0.3, indicating the presence of another nanoporous window, which agreed with the mesoporous peak at 2.6 nm in Figure 4b. The secondary uptake of BNOC-30 seen from P/P_0=0.01 to P/P_0=0.5, indicated larger nanopores than in BNOC-20 (in according with the existence of two peaks at 3.2 and 4.0 nm in the pore size distribution). As regard to BNOC-40, type IV isotherm was observed with a H3 hysteresis loop, indicating clear existence of large slit mesopores (as agree with pore sizes peaking at 3.7 nm and 5.1 nm in Figure 4b). Thus, it is easily seen from Figure 4b that all the BNOCs exhibited hierarchical porous structures. The micropore sizes of BNOCs could be adjusted from 1.35 to 1.78 nm, and the mesopore sizes varied from 2.3 to 5.1 nm, by increasing the E&D time.

The textural parameters including specific surface area (S_{BET}), total pore volume (V_p), micropore area (S_{micro}), mesopore area (S_{meso}), micropore volume (V_{micro}), and mesopore volume (V_{meso}) of BNOCs are presented in Figure 4c,d and Table 1. BNOC-10 was mainly composed of micropores. Thus, it exhibited the highest S_{micro} (1145.6 m^2 g^{-1}) and V_{micro} (0.397 cm^3 g^{-1}), but the smallest V_p (0.450 cm^3 g^{-1}), S_{meso} (59.6 m^2 g^{-1}), and V_{meso} (0.052 cm^3 g^{-1}). With the increase of E&D time, V_p, S_{meso}, and V_{meso} showed a continuous increase with the increase of reaction time, while S_{micro} and V_{micro} exhibited a step-by-step decrease. When the CVE&D time reached 40 min, the pore volume went up to 1.52 cm^3 g^{-1} and the most of the contribution was provided by mesopores (91.5%). This result

indicated that many mesopores were generated, while some micropores were etched out. BNOC-20 hold the highest surface area (1456.4 $m^2 g^{-1}$), and the surface area of BNOC-10, BNOC-30 and BNOC-40 decreased to 1205.2 $m^2 g^{-1}$, 1382.5 $m^2 g^{-1}$ and 1149.4 $m^2 g^{-1}$, respectively. Therefore, it's concluded that ammonia gas and boric acid etched carbon at 1000 ^oC and generated mesopores. With the reaction time increasing, the size of mesopores also gradually and controllably increased. The contribution of mesopores to the specific surface areas arose with the increase of CVE&D time as well. However, since more and more carbon species with micropores were etched out, the contribution of micropores to the total surface area decreased with the increase of reaction time. Thus, the maximum specific surface area was natural to BNOC-20. In brief, the pores of BNOC membranes were hierarchically structured, with micropore size ranging from 1.35 to 1.78 nm and mesopore size adjustable within a range of 2.3 to 5.1 nm, which was well controllable by CVE&D time.

Growth process of chemical vapor etching & doping for BNOCs

The detailed "chemical vapor etching & doping" (CVE&D) process of converting cellulose-made paper into B, N, O co-doped 3D nanoporous carbon microfiber networks (BNOCs) is illustrated in Figure 5. First of all, the papers which are made of α-cellulose were carbonized when the temperature reached 1000 ^oC. The network morphology was well maintained when cellulose was carbonized into carbon (Equation 1), while solid carbon fibers with smooth surface (seen from the SEM images, Figure S1a and b) and turbostratic graphite structure (confirmed by the Raman spectra, Figure S1c) were generated, as confirmed by paper annealing at 1000 ^oC in Ar atmosphere for 30 min

(Denoted as C-30). However, those carbon networks showed a low surface area of 867.8 m^2 g^{-1}, where 95% of the surface area was contributed from micropores (Figure S1d and Table 1). During the CVE&D process, vaporized boric acid carried by flowing ammonia gas reacted with the obtained carbon micro-fibers following the reaction described by Equation 2 and 3[44, 49]. The gas-phase product left away with the carrying gas and generated abundant nano-pores, leaving hierarchical porous carbon fiber networks composed of crystallized ultrathin carbon sheets. This technology can also guaranteed a homogeneous *in-situ* B, N, and O doping inside each crystal along with the reactions:

$$(C_6H_{10}O_5)_x \xrightarrow{1000\ ^\circ C} C + H_2O \quad (1)$$

$$NH_3 + C \rightarrow CH_4 + N_2 + C_xN_y \quad (2)$$

$$H_2BO_3 + C \rightarrow H_2O + CO + C_xB_yO_z \quad (3)$$

Supercapacitive properties of BNOCs

The microfiber-network structure of BNOCs provides a multi-dimensional interconnected electron freeway, ensuring from a fast electron transfer.[54] Besides, their huge surface areas of up to 1456 m^2 g^{-1}, contributed by the abundant micropores can effectively adsorb ions, while the controllable mesopores enable quick ion diffusion[7], being in favor of application in supercapacitors. Given this, we investigated their capacitive properties in a 1 M H_2SO_4 aqueous electrolyte using a two electrode setup reflecting the electrochemical performance of a real capacitor.[55]. In the cyclic voltammetric (CV) curves of BNOC-based supercapacitors (Figure 6a, Figure S3), their

rectangular shapes indicated the near-ideal capacitive electrical double layer behavior with small equivalent series resistance and high equivalent parallel resistance. Comparing with the undoped sample (C-30) and a previous carbon-type AC based supercapacitor (Figure S3d), whose capacitances decreased dramatically at high scan rates, the BNOC electrodes retained their high capacitance values and rectangular shape even at the ultrahigh scan rates up to 200 mV s^{-1}.

Then, under the current density ranging from 0.1 to 200 A g^{-1}, we investigated the galvanostatic charge/discharge (GCD) curves of BNOCs *vs.* C-30 and AC performances (Figure S4). We calculated their associated specific capacitances by means of their GCD at different current densities (Figure 6c). At 0.1 A g^{-1}, BNOC-30 showed the highest capacitance of 357 F g^{-1}, among all the BNOC samples (e.g., BNOC-10, BNOC-20 and BNOC-40, which also revealed rather high values of 236, 308 and 263 F g^{-1}, respectively). This number is 2.5 times higher than that of AC and 1.7 times higher than that of C-30. The result indicated that the final specific capacitances of BNOCs are not only dependent on their samples' specific surface areas. For example, BNOC-20 holded the highest surface area but BNOC-30 exhibited the highest specific capacitance. Considering that the B, N, and O contents of BNOC-30 are much higher than those in BNOC-20, we believe that the hetero-atom doping played an important part in improving the capacitance by introducing additional high pseudocapacitance.

The capability of retaining high capacitance during ultrafast charging/discharging current is critical for high-performance supercapacitor devices. The powder nature of AC resulted high contact resistance as well as limited ion diffusion, and therefore, the specific

capacitance of the AC based supercapacitor dropped rapidly from 142.8 F g^{-1} at 0.1 A g^{-1} to 10 F g^{-1} at 50 A g^{-1}, and no capacitance was maintained at a higher current density of 100 A g^{-1}. The undoped sample (C-30) exhibited no better performance, whose capacitance could only be measured at current densities below 10 A g^{-1} and dropped rapidly from 211.6 F g^{-1} at 0.1 A g^{-1} to 64 F g^{-1} at 10 A g^{-1}. The microfiber network structure of BNOCs allows fast electron transfer through the interconnected network and the abundant mesopores ensure effective ion diffusion. Thus, all the BNOC samples could applied in supercapacitors with high charge/discharge current density of 100 A g^{-1}. It is noticeable that the capacitance retentions of BNOCs increased with the increasing amount and size of mesopores. With the minimum mesopores (11.5 %) and the smallest mesopore size (2.3 nm), BNOC-10 retained 20% of its initial capacitance when the current density was increased up to 100 A g^{-1}. BNOC-20 had more mesopores (52.0 %) and larger mesopore size (2.6 nm), and its capacitance retention at 100 A g^{-1} was increased to 44 %. With the further increased amount of mesopores (78.5 %) and their much larger pore size (3.5 nm), BNOC-30 retained 51% of its initial capacitance at 100 A g^{-1}. Noticeably, the capacitance of BNOC-30 decreased slowly to 150 F g^{-1} at a high current density of 200 A g^{-1}, indicating its excellent power capability. Such outstanding rate capability is attributed to the two inherent factors of the BNOC samples: fast ion diffusion rate caused by the optimized hierarchical porous structures[7] and small electron transfer resistance provided by the cross-linked 3D network structure[54]. BNOC-40 held the highest ratio of mesopores (91.4 %) and the largest pore size (5.1 nm), but the ratio of capacitance retention was the same with BNOC-30, indicating that the rate of ion diffusion in BNOC-30 had reached

the maximum, while further increase of pore volume and pore size would not benefit the ion diffusion anymore.

Figure 6b illustrates comparative GCD curves of BNOCs *vs.* AC at a current density of 10 A g^{-1}. The BNOC-20-, BNOC-30- and BNOC-40-based supercapacitors showed ideal linear and symmetrical profiles without obvious IR drops. By contrast, the AC based supercapacitor revealed a large IR drop of 0.12 V and C-30 based supercapacitor exhibited an IR drop of 0.52 V at a current density of 10 A g^{-1}. The initial voltage drops were proportional to the discharge currents (Figure 6d), determining the direct current internal resistances ($R_{i,DC}$), which reflects the electron transfer resistance in the active materials and ion diffusion resistance in the electrolyte.[35] The $R_{i,DC}$ of BNOC-30 was only 0.6 Ω , which is one fifth of that of AC (3.1 Ω), indicating that they may deliver extremely high discharge power. Electrochemical Impedance Spectroscopy (EIS) was then employed to analyze the electrochemical behavior. As shown in Figure 6e, there were three critical factors in the equivalent circuits of BNOC-30 and AC: (i) the series resistance (R1) which reflected the electron transfer resistance between current collector and carbon material and the ionic resistance of the bulk electrolytes; R1 of BNOC-30 was 0.38 Ω, smaller than that of AC (0.47 Ω), indicating the better conductivity of BNOC-30; (ii) the channel resistances inside the cavities (R2) reflecting the ionic resistances of electrolytes inside the pores; R2 was only 0.19 Ω for BNOC-30 and increased to 0.34 Ω for AC based supercapacitor, which reflecting fast ion transfer in the pores of BNOC-30; (iii) the contact resistances of electrode materials (R3). BNOC-30 had an interconnected network structure, which provided a perfect pathway for electron transfer. Therefore, the resistance within the electrode materials was only 0.27 Ω for BNOC-30. However, R3

was 1.45 Ω for AC, owing to the massive interparticle contact resistances. Such small R1, R2 and R3 values of BNOC-30 resulted in a low initial voltage drop of BNOC-based supercapacitor and higher available output power and energy[20] , as summarized in the Ragone Plots (Figure 6f). Especially for the BNOC-30-based supercapacitors, their available power density can reach 102.4 kW kg^{-1}, while the maximum power density (P_{max}) of BNOC-30 can reach 300.6 kW kg^{-1}, which is very close to an aluminum electrolytic capacitor,[20, 56]and surpasses most of EDLSs based on 3D carbon fiber networks[13, 57, 58], 3D graphene,[11, 18, 56] graphene–cellulose papers,[59] 3D RGO hydrogels,[11, 28] CNT/graphene hybirds,[17, 60, 61] and other 3D carbon architectures[23, 29, 30, 32, 34, 49, 62]. The unique structure of BNOCs also enabled them great cycling stability. As shown in Figure S5, the cycling stability was evaluated for 10000 charge-discharge cycles at a current density of 100 A g^{-1}. Capacitive retention was found to be nearly 100% even at such high charge-discharge current density. And the last ten cycles still displayed the same symmetrical triangular shape, indicating excellent cyclability.

All solid state supercapacitor based on BNOC-30

Aiming at the development of a power source with good electrochemical and well-flexible properties, we fabricated a symmetric flexible ASSS assembled with BNOC-30 as flexible electrodes(Figure 7a). two kind of gel electrolytes (PVA/H_2SO_4 gel[63] and PPDP/LiCl[64]) were chosen as the solid-state electrolytes. PVA/H_2SO_4 gel is the most commonly used solid state electrolyte. However, in contrast to the supercapacitors with liquid electrolyte, whose CV curves retained their high capacitance values and rectangular shape even at scan rates of up to 200 mV/s (Figure 6a), the capacitance of ASSS based on

PVA/H_2SO_4 gel electrolyte exhibited a relatively quick drop with the increase of scan rates (Figure 7b). Such decrease of capacitance is usually attributed to the discrepant insertion/deinsertion behaviors of ions from electrolyte to the active materials.[63, 65] However, considering the abundant mesopores in BNOC-30, which acts as effective ion diffusion pathways, the decrease may be attributed to the slow ion-transport inside the solid state electrolyte as well. To confirm this assumption, ASSS was test with PPDP/LiCl gel electrolyte, which has the ability of bringing ion migration channels to the ions and allows more effective ion diffusion in electrolyte. As shown in Figure 7c, the ASSS with PPDP/LiCl gel electrolyte retained its high capacitance values and nearly rectangular shape even at ultrahigh scan rates up to 100 mVs^{-1}, suggesting their high-rate capability due to the effective ion diffusion. The capacitances obtained by the galvanostatic charge/discharge measurements at a current density between 1 and 10 A g^{-1} (Figure S8) are plotted in Figure 7d. ASSS in PPDP/LiCl gel electrolyte illuminated much higher capacitances than that in PVA/H_2SO_4 gel electrolyte. A high capacitance of 242.4 F g^{-1} was obtained at a current density of 1 A g^{-1} in PPDP/LiCl gel electrolyte, which is also much higher than that in PVA/H_2SO_4 gel electrolyte, surpassing the ASSSs based on activated carbon cloths,[66] graphite hybrid,[61] carbon nanotube[67] and B, N co-doped graphene[11]. Moreover, for ASSS in PPDP/LiCl gel electrolyte, 71.6% of its initial capacitance was still retained at 10 A g^{-1}, which is also much better than that of PVA/H_2SO_4 gel electrolyte (58% capacitance retention at 10 A g^{-1}), indicating good rate property. The highest energy density in PPDP/LiCl gel electrolyte is 8.4 Wh kg^{-1} at the power density of 125 W kg^{-1} (Figure S12, Supporting Information) which is comparable with those of other reports[61, 66, 67]. EIS measurements were also carried out. As shown in

Figure 7e, the Nyquist plots were composed of two distinct parts, a straight line in low frequency region and a semicircle in the high frequency region. The diameter of the semicircle corresponds to the charge transfer resistance (R_{ct}). It is obviously seen that PPDP/LiCl gel electrolyte had smaller R_{ct}. And the linear parts at low frequency corresponds to the diffusion process of the electrolyte ions. The slope of PPDP/LiCl gel electrolyte was relative steeper than that of PVA/H_2SO_4 gel electrolyte, indicating higher ion diffusion rate. Therefore, our results demonstrated that, besides the inner pore ion diffusion, the ion diffusion in the electrolyte is also a limiting factor toward high performance ASSSs. Gel electrolyte with better ion diffusion helps to achieve a good performance as well.

The as-prepared ASSSs also exhibited excellent flexibility and stability as demonstrated in Figure 7f. Compared with the non-bending CV curve at a sweep rate of 100 mV s^{-1}, BNOC-30 based ASSS preserved nearly unchanged CV curves at different bending curvatures of 60, 120, and 180º, accounting for a constant capacitance output under any degree of extreme bending condition. More strikingly, 100-cycles tests with the bending angles of 180° never affected its structural integrity and did not weaken its storage performance, reflecting high flexible and recoverable abilities. Additionally, the stability tests (Figure S6) showed that the ASSSs could still maintain a high percentage of their initial capacitances after 10000-cycles of charge-discharge processes. Such excellent bending and cycling stability was rooted in the mechanically outstanding integrity of interpenetrating-fiber-network BNOC-30 structures, as well as in the excellent interconnected integrity between BNOC-30 and the gel electrolyte.[6] To further demonstrate the practical usage of the flexible ASSSs based on BNOCs, several ASSS

units were serial and parallel connected. CV and GCD measurements (Figure S13) show that the potential window was extended from 1.0 V for ASSS unit to 4.0 V for the tandem device with four ASSSs in series. And the capacitance doubled when two sets of four series ASSSs are in parallel connection. It is worth mentioning that with serial and parallel connections of several ASSSs, the resultant device can successfully light a blue-light-emitting diode (LED) (Movie S2).

Conclusion

In summary, from a synthetic perspective, we successfully developed a novel one-step chemical vapor etching and synchronously doping route to achieve the scalable heteroatom-doped 3D interconnected carbon microfiber networks, by using easy-to-get cellulose papers as precursors. Special continuous network morphologies, adjustable hierarchical porous structures, and controllable elemental contents, which are decently suitable for electrochemical storage, were the created features of the 3D BNOCs samples. The inherently interconnected fiber network structure provides good conductivity through organizing an electron highway. The mesopores provide high surface area needed for efficient ion adsorption. The abundant mesopores and macropores are helpful for ion diffusion. And the B, N and O dopants induce high pseudocapacitance. All these parameters make BNOCs remarkable electrode materials for aqueous and flexible all-solid-state supercapacitor devices.

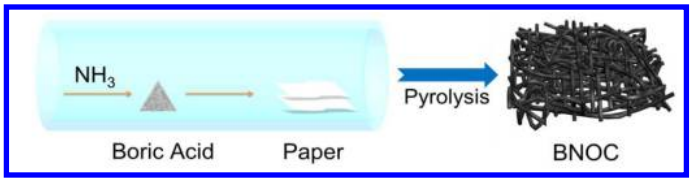

Figure 1 Schematic diagram illustrating the synthetic strategy of BNOCs.

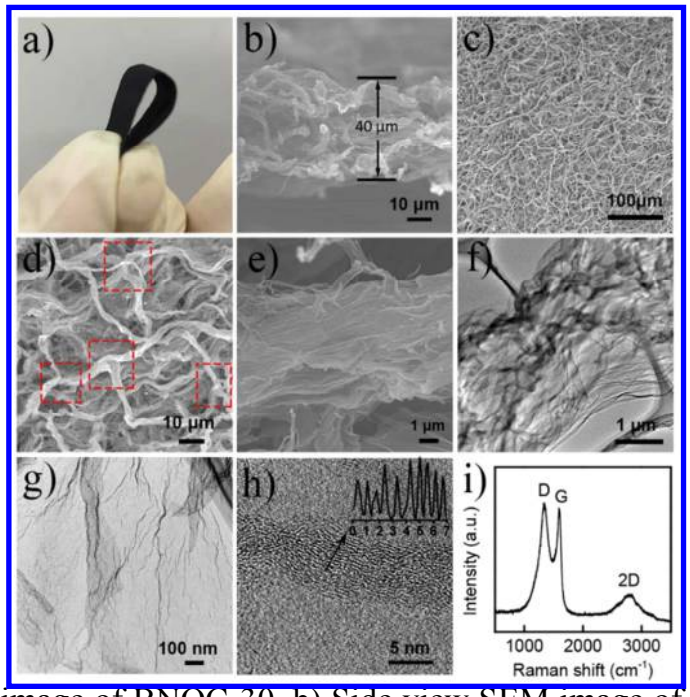

Figure 2 a) Digital image of BNOC-30. b) Side view SEM image of BNOC-30. c), d), e) Top view SEM images of BNOC-30 under different magnifications. f), g), h) TEM images of BNOC-30 at different magnifications. The inset in h) shows the contrast intensity profile recorded along the arrows. i) Raman spectrum of BNOC-30.

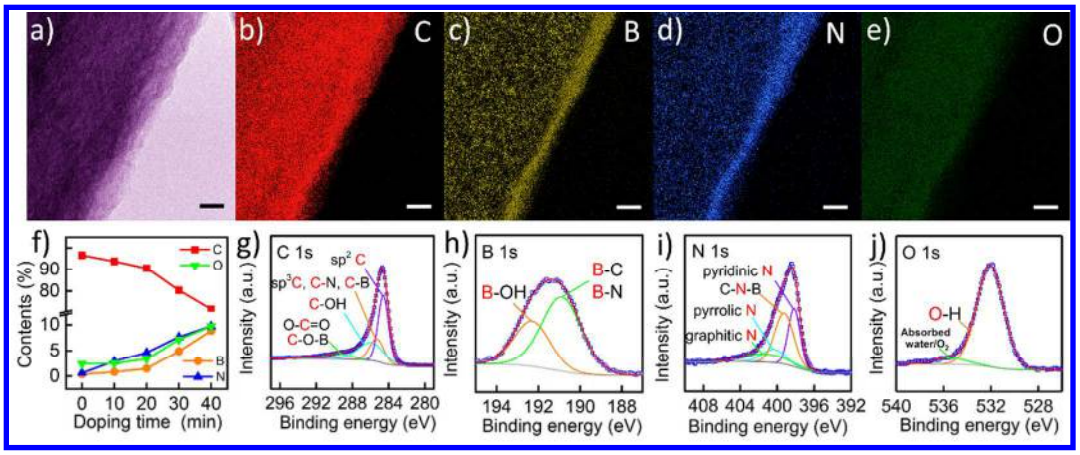

Figure 3 a) Representative energy filtered TEM (EFTEM) image of BNOC-30, scale bar is 20 nm. b-e) EELS elemental maps of C, B, N, O. f) Atomic contents of B, N, O and C at different doping times. g-j) High-resolution C1s spectrum, B 1s spectrum, N 1s spectrum and O 1s spectrum of BNOC-30.

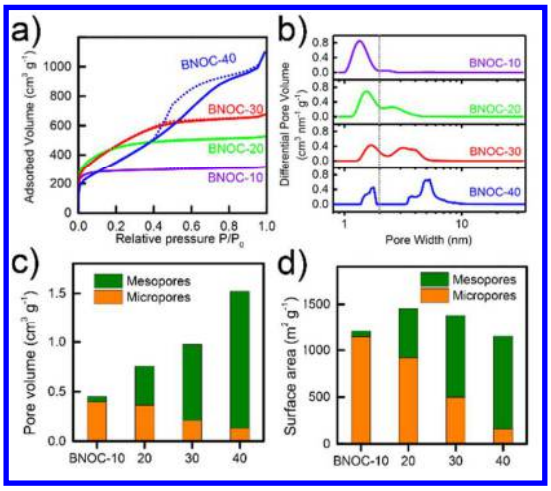

Figure 4 a) Nitrogen adsorption–desorption isotherms of BNOCs. b) Pore size distribution of BNOCs using the quenched solid state functional theory. c), d) Total pore volume and specific surface area comparison of BNOCs.

Table 1 The textural parameters (including S_{BET}, V_p, S_{micro}, S_{meso}, V_{micro}, V_{meso}) of the BNOCs and C-30.

Sample	S_{BET} ($m^2\ g^{-1}$)	V_p ($cm^3\ g^{-1}$)	S_{micro}/S_{meso} ($m^2\ g^{-1}$)	V_{micro}/V_{meso} ($cm^3\ g^{-1}$)
BNOC-10	1205.2	0.450	1145.6/59.6	0.397/0.052
BNOC-20	1456.4	0.757	917.1/539.3	0.363/0.394
BNOC-30	1382.5	0.973	498.0/884.4	0.210/0.764
BNOC-40	1149.4	1.520	158.9/990.5	0.130/1.390
C-30	867.8	0.330	822.9/44.9	0.257/0.073

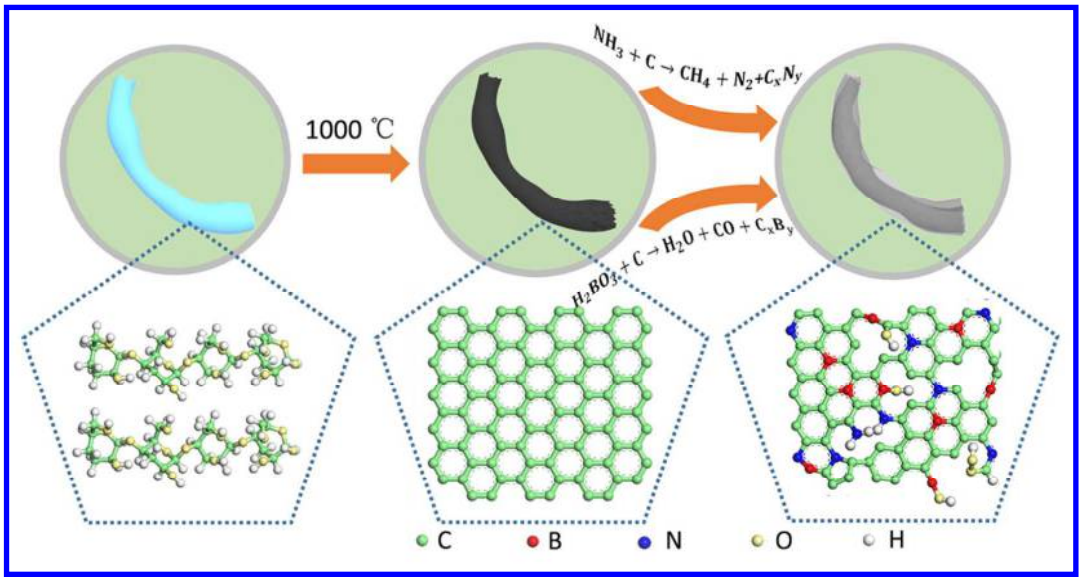

Figure 5 Schematic diagram showing the reaction process under the developed chemical vapor etching & doping strategy.

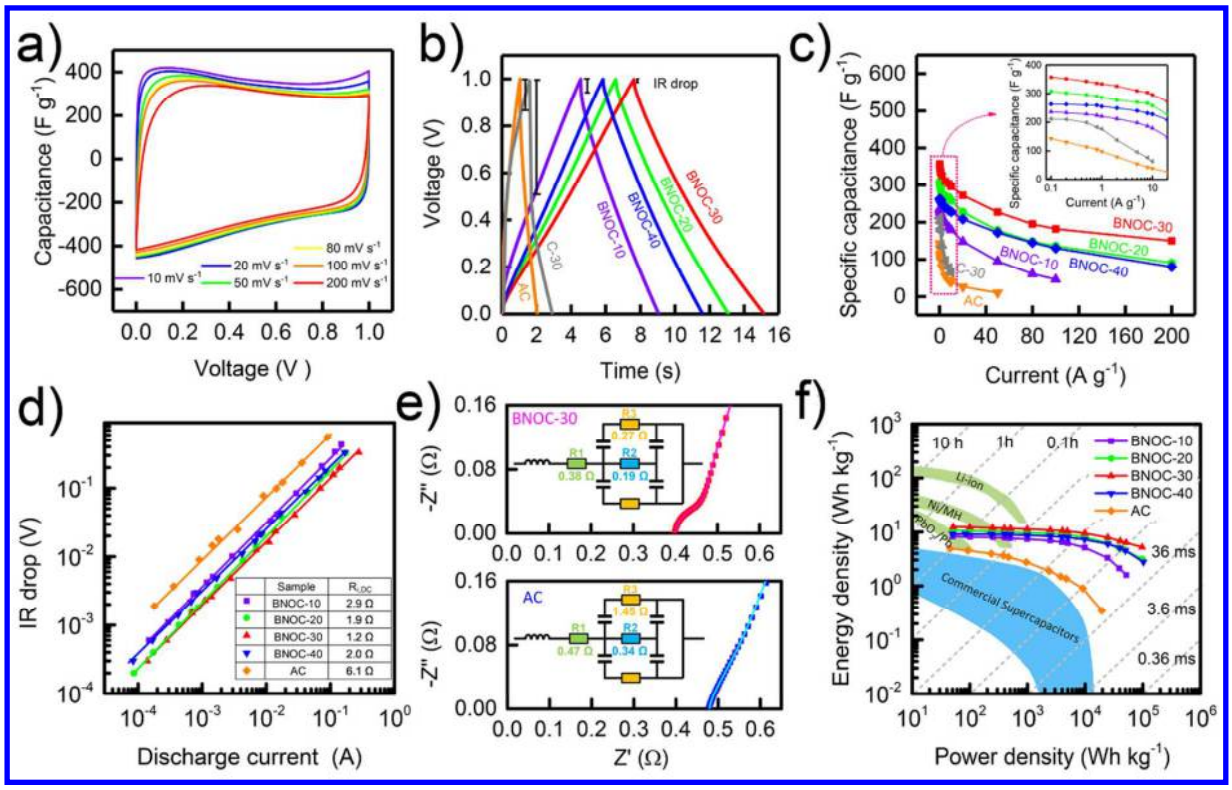

Figure 6 a) CV curves of BNOC-30 at different scan rates. b) GCD profiles of BNOC-10, BNOC-20, BNOC-30, BNOC-40, C-30 and AC at a current density of 10 A g^{-1}. c) Specific capacitance of BNOC-10, BNOC-20, BNOC-30, BNOC-40, C-30 and AC as a function of current densities. The inset shows the magnifying figure of curves in the red frame. d) Initial voltage drops of BNOCs and AC at different galvanostatic discharge currents. e) High frequency regions of the Nyquist plots of BNOC-30 (top) and AC (bottom) and the corresponding equivalent circuits. f) Ragone plots of BNOCs and AC based supercapacitors.

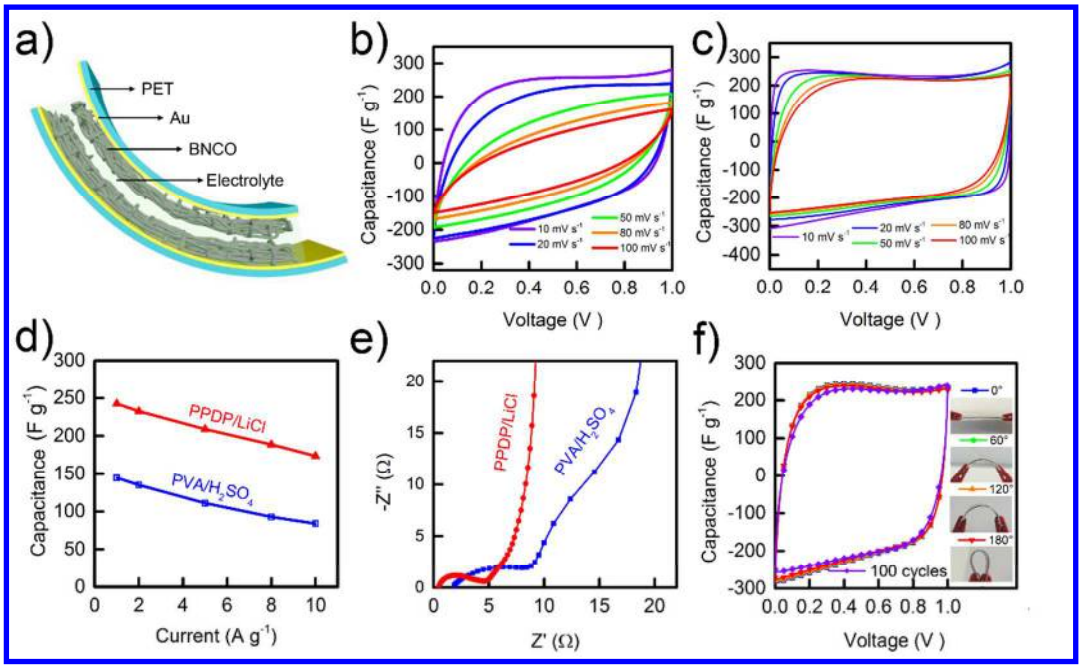

Figure 7 a) Schematics of the stacked ASSS. b) CV curves of ASSS with PVA/H_2SO_4 electrolyte scanned from 10 mV s^{-1} to 100 mV s^{-1}. c) CV curves of ASSS with PPDP/LiCl electrolyte scanned from 10 mV s^{-1} to 100 mV s^{-1}. d) Specific capacitances as a function of current densities. e) Nyquist plots of ASSS with PVA/H_2SO_4 and PPDP/LiCl electrolyte. f) CV curves at different bending angles with scan rate of 100 mV s^{-1}.

Experimental section

Synthesis of BNOCs

Filtering papers (99% α-cellulose, Whatman) were put in the high-temperature zone of a tubular furnace, while boric acid (2g) was put in the low-temperature area of the furnace. After filling with ammonia gas, the temperature was raised to 1000 ^{o}C at a heating rate of 40 ^{o}C /min and then kept for 10 to 40 min. The exhaust was cooled by water to absorb the remaining ammonia gas and gas-phase products. Afterward, argon (Ar) was filled into the tube instead of ammonia gas and the furnace was cooled down to room temperature. The obtained films were washed with hot water and dried at 200 ^{o}C in a constant temperature oven. BNOCs with different specific surface areas, pore size distributions and elemental contents were fabricated by adjusting the CVE&D time from 10 min, 20 min, 30 min to 40 min. For comparison, The undoped sample (C-30) was prepared by pyrolyzing filtering papers in Ar at 1000 ^{o}C for 30 min.

Characterizations

The morphologies of BNOCs were visualized by scanning electron microscopy (JEOL JSM-6700F) and high resolution transmission electron microscopy (JEOL JEM-3000F). The crystal structures were characterized by Raman spectroscopy (HORIBA Jobin Yvon T6400) and electron energy loss spectroscopy (EELS, attachment of JEOL JEM-3000F). The analysis of compositions and chemical states was carried out using an X-ray photoelectron spectrometer (XPS, Thermo Scientific Escalab 250Xi) and elemental analyzer (elementar vario MICRO cube). The N_2 adsorption–desorption isotherms were obtained using an automated gas sorption instrument (Quantachrome Autosorb-IQ2

System) at 77 K. The total surface area was calculated using Brunauer-Emment-Teller (BET) method and the pore size distribution (PSD) was obtained from the adsorption branch of the isotherm based on the quenched solid density functional theory (QSDFT).

Electrochemical measurements

The electrochemical studies were first carried out in a two-electrode system with the H_2SO_4 aqueous solution (1 M) as the electrolyte. This two electrode configuration consists of two pieces of free-standing BNOCs with the same size (1cm x 1cm) as electrode materials, filtering paper (pore size of 225 nm) as the separator and a pair of Au foils as the current collectors. The as-assembled devices were soaked in the electrolyte for 10 min and wrapped with parafilm before test. For a solid state supercapacitor, a PVA/H_2SO_4 gel electrolyte was prepared as follows: 6 g of H_2SO_4 was mixed with 60 ml of DI water, and then 6 g of polyvinyl alcohol (PVA) was added. The whole mixture was heated to 85 ^{o}C under stirring till the solution became clear. PPDP/LiCl gel electrolyte was prepared as follows: 1.0 g propylsulfonate dimethylammonium propylmethacrylamide (PDP), 1.0 mg 4,4'-azobis(4-cyanovaleric acid) (ACVA) and 4.0 ml distilled water were mixed in a sealed round-bottom reactor, following with three times of frozen–degassing–thawing cycles to remove the gas. The reactor was put in oil bath at 70 °C for 10 h to form PPDP. Afterwards, the as-prepared PPDP was mixed homogeneously with 6.0 ml aqueous solution including 1.0 g $LiCl{\cdot}H_2O$ to obtain the PPDP/LiCl gel. Two pieces of BNOC-30 (1cm x 1cm) were immersed in the hot electrolyte for 2 min and transferred onto two gold coated PET sheets, which were used as the flexible substrate and current collector. The electrode with a thin solution coating

layer was left in the fume hood for 24 h to vaporize the water. Then, two pieces of the electrodes were pressed together to assemble a supercapacitor.

All electrochemical measurements were carried out on a CHI 660E electrochemical workstation at room temperature, including cyclic voltammetry (CV), chronopotentiometry and electrochemical impedance spectrometry (EIS). Gravimeteric specific capacitance (C, F g^{-1}) was calculated from galvanostatic charging/discharging using the following equation:

$$C = \frac{4I}{m(dV/dt)} \quad (1)$$

Where I is the constant current applied in the discharging process (A); m is the overall mass of two active electrodes (g); dV/dt is the slope of the discharge curves (V s^{-1}).

The direct-current equivalent internal resistance ($R_{i,DC}$, Ω) was obtained by:

$$R_{i,DC} = \frac{V_{drop}}{2I} \quad (2)$$

Where V_{drop} is the initial voltage drop at the beginning of discharge (V).

The energy density (E, Wh kg^{-1}) was determined using an equation:

$$E = \frac{CV^2}{8} \quad (3)$$

Where V is the effective potential range during discharge.

The power density (P, W kg^{-1}) was calculated by:

$$P = \frac{3600E}{t} \quad (4)$$

Where t is the discharging time (s).

The maximum power density (P_{max}, W kg^{-1}) was determined by:

$$P_{max} = \frac{V_{OCV}^2}{4mR_{i,DC}} \quad (5)$$

Where V_{OCV} is the open circuit voltage (V).

ASSOCIATED CONTENT

Supporting Information.

SEM images, Raman spectrum, nitrogen adsorption-desorption isotherm and pore size distribution of filter paper carbonized at 1000 ^{o}C in Ar; XPS survey spectra of BNOCs at different doping time; CV curves of BNOCs and AC at different scan rate; The galvanostatic charge/discharge (GCD) curves of BNOCs and AC at charge/discharge current density ranging from of 0.1A/g to 200 A/g; Cycling stability measurement of EDLS based on BNOC-30 at 100 A/g; Cycling stability measurement of based on ASSS at 1 A/g; XRD pattern of BNOCs; The galvanostatic charge/discharge (GCD) curves of BNOC-based ASSSs with different electrolytes; SEM and TEM images of BNOC-30; Comparison of the supercapacitor performance of this work and other recent works; SEM images, XRD patterns and XPS spectra of BNOC-30 after cycling test; Ragone plots of ASSS with PVA/H_2SO_4 and PPDP/LiCl electrolyte; Movies

showing the flexibility of BNOC-30 and the demonstration device with serial and parallel connections of ASSSs. (PDF)

AUTHOR INFORMATION

Corresponding Author

***E-mail:** ym.xue@hebut.edu.cn

***E-mail:** wangxb@nju.edu.cn

***E-mail:** zhaoxuebo@upc.edu.cn

Author Contributions

The manuscript was written through contributions of all authors. All authors have given approval to the final version of the manuscript. P.D., Y.X. and X.Z. conceived the project and prepared the manuscript. S.Z. assisted in fabricating devices. L.C. carried out the device fabrication of ASSS. D.T. performed the TEM measurement. X.G. performed the SEM measurement. L.L. carried out the Raman measurement and analysed data. X.W. assisted in analyzing the electrochemical measurement. X.J. conducted EIS measurement and data analysis. D.L. drew the schematic diagram. L.K. performed the Nitrogen adsorption–desorption measurement. All authors discussed the results and commented on the manuscript. Y.B., D.G. and X.Z. supervised the project.

ACKNOWLEDGMENT

This work was supported by Natural Science Foundation of China (21473254 and 51702365), the Special Project Fund of “Taishan Scholars” of Shandong Province (NO.ts201511017), the Fundamental Research Funds for the Central Universities (16CX05006A), New Faculty Start-up

funding in China University of Petroleum (East China) (YJ201501029), the Australian Research Council for granting a Laureate Fellowship (Grant No. FL 160100089), and the World Premier International Center for Materials Nanoarchitectonics (WPI-MANA) of NIMS, Tsukuba, Japan.

REFERENCES

1. Jiang, H.; Lee, P. S.; Li, C., 3d Carbon Based Nanostructures for Advanced Supercapacitors. *Energy Environ. Sci.* **2013,** *6*, 41-53.
2. Chen, H.; Cong, T. N.; Yang, W.; Tan, C.; Li, Y.; Ding, Y., Progress in Electrical Energy Storage System: A Critical Review. *Prog. Nat. Sci.* **2009,** *19*, 291-312.
3. Niu, J.; Shao, R.; Liang, J.; Dou, M.; Li, Z.; Huang, Y.; Wang, F., Biomass-Derived Mesopore-Dominant Porous Carbons with Large Specific Surface Area and High Defect Density as High Performance Electrode Materials for Li-Ion Batteries and Supercapacitors. *Nano Energy* **2017,** *36*, 322-330.
4. Wang, G.; Zhang, L.; Zhang, J., A Review of Electrode Materials for Electrochemical Supercapacitors. *Chem. Soc. Rev.* **2012,** *41*, 797-828.
5. Choi, H.-J.; Jung, S.-M.; Seo, J.-M.; Chang, D. W.; Dai, L.; Baek, J.-B., Graphene for Energy Conversion and Storage in Fuel Cells and Supercapacitors. *Nano Energy* **2012,** *1*, 534-551.
6. Chen, L.-F.; Huang, Z.-H.; Liang, H.-W.; Yao, W.-T.; Yu, Z.-Y.; Yu, S.-H., Flexible All-Solid-State High-Power Supercapacitor Fabricated with Nitrogen-Doped Carbon Nanofiber Electrode Material Derived from Bacterial Cellulose. *Energy Environ. Sci.* **2013,** *6*, 3331.
7. Zhang, L. L.; Zhao, X. S., Carbon-Based Materials as Supercapacitor Electrodes. *Chem. Soc. Rev.* **2009,** *38*, 2520-2531.
8. Staaf, L. G. H.; Lundgren, P.; Enoksson, P., Present and Future Supercapacitor Carbon Electrode Materials for Improved Energy Storage Used in Intelligent Wireless Sensor Systems. *Nano Energy* **2014,** *9*, 128-141.
9. Jiang, X.-F.; Wang, X.-B.; Dai, P.; Li, X.; Weng, Q.; Wang, X.; Tang, D.-M.; Tang, J.; Bando, Y.; Golberg, D., High-Throughput Fabrication of Strutted Graphene by Ammonium-Assisted Chemical Blowing for High-Performance Supercapacitors. *Nano Energy* **2015,** *16*, 81-90.
10. Faraji, S.; Ani, F. N., The Development Supercapacitor from Activated Carbon by Electroless Plating—a Review. *Renew. Sust. Energ. Rev.* **2015,** *42*, 823-834.
11. Wu, Z.-S.; Winter, A.; Chen, L.; Sun, Y.; Turchanin, A.; Feng, X.; Müllen, K., Three-Dimensional Nitrogen and Boron Co-Doped Graphene for High-Performance All-Solid-State Supercapacitors. *Adv. Mater.* **2012,** *24*, 5130-5135.
12. Cong, H.-P.; Ren, X.-C.; Wang, P.; Yu, S.-H., Flexible Graphene-Polyaniline Composite Paper for High-Performance Supercapacitor. *Energy Environ. Sci.* **2013,** *6*, 1185-1191.
13. Cheng, Y.; Huang, L.; Xiao, X.; Yao, B.; Yuan, L.; Li, T.; Hu, Z.; Wang, B.; Wan, J.; Zhou, J., Flexible and Cross-Linked N-Doped Carbon Nanofiber Network for High Performance Freestanding Supercapacitor Electrode. *Nano Energy* **2015,** *15*, 66-74.
14. Wang, D.-W.; Li, F.; Liu, M.; Lu, G. Q.; Cheng, H.-M., 3d Aperiodic Hierarchical Porous Graphitic Carbon Material for High-Rate Electrochemical Capacitive Energy Storage. *Angew. Chem. Int. Ed.* **2008,** *47*, 373-376.

15. Jiang, H.; Lee, P. S.; Li, C., 3d Carbon Based Nanostructures for Advanced Supercapacitors. *Energy Environ. Sci.* **2013,** *6*, 41-53.
16. Zhu, Y.; Murali, S.; Stoller, M. D.; Ganesh, K. J.; Cai, W.; Ferreira, P. J.; Pirkle, A.; Wallace, R. M.; Cychosz, K. A.; Thommes, M.; Su, D.; Stach, E. A.; Ruoff, R. S., Carbon-Based Supercapacitors Produced by Activation of Graphene. *Science* **2011,** *332*, 1537-1541.
17. Fan, Z.; Yan, J.; Zhi, L.; Zhang, Q.; Wei, T.; Feng, J.; Zhang, M.; Qian, W.; Wei, F., A Three-Dimensional Carbon Nanotube/Graphene Sandwich and Its Application as Electrode in Supercapacitors. *Adv. Mater.* **2010,** *22*, 3723-3728.
18. Shao, Y.; El-Kady, M. F.; Lin, C. W.; Zhu, G.; Marsh, K. L.; Hwang, J. Y.; Zhang, Q.; Li, Y.; Wang, H.; Kaner, R. B., 3d Freeze-Casting of Cellular Graphene Films for Ultrahigh-Power-Density Supercapacitors. *Adv. Mater.* **2016,** *28*, 6719-26.
19. Xu, J.; Tan, Z.; Zeng, W.; Chen, G.; Wu, S.; Zhao, Y.; Ni, K.; Tao, Z.; Ikram, M.; Ji, H.; Zhu, Y., A Hierarchical Carbon Derived from Sponge-Templated Activation of Graphene Oxide for High-Performance Supercapacitor Electrodes. *Adv. Mater.* **2016,** *28*, 5222-5228.
20. Wang, X.; Zhang, Y.; Zhi, C.; Wang, X.; Tang, D.; Xu, Y.; Weng, Q.; Jiang, X.; Mitome, M.; Golberg, D.; Bando, Y., Three-Dimensional Strutted Graphene Grown by Substrate-Free Sugar Blowing for High-Power-Density Supercapacitors. *Nat. Commun.* **2013,** *4*, 2905.
21. Zhao, J.; Jiang, Y.; Fan, H.; Liu, M.; Zhuo, O.; Wang, X.; Wu, Q.; Yang, L.; Ma, Y.; Hu, Z., Porous 3d Few-Layer Graphene-Like Carbon for Ultrahigh-Power Supercapacitors with Well-Defined Structure–Performance Relationship. *Adv. Mater.* **2017,** *29*, 1604569.
22. Qin, T.; Wan, Z.; Wang, Z.; Wen, Y.; Liu, M.; Peng, S.; He, D.; Hou, J.; Huang, F.; Cao, G., 3d Flexible O/N Co-Doped Graphene Foams for Supercapacitor Electrodes with High Volumetric and Areal Capacitances. *J. Power Sources* **2016,** *336*, 455-464.
23. Chen, L.-F.; Huang, Z.-H.; Liang, H.-W.; Gao, H.-L.; Yu, S.-H., Three-Dimensional Heteroatom-Doped Carbon Nanofiber Networks Derived from Bacterial Cellulose for Supercapacitors. *Adv. Funct. Mater.* **2014,** *24*, 5104-5111.
24. Yu, X.; Kang, Y.; Park, H. S., Sulfur and Phosphorus Co-Doping of Hierarchically Porous Graphene Aerogels for Enhancing Supercapacitor Performance. *Carbon* **2016,** *101*, 49-56.
25. Qie, L.; Chen, W.; Xu, H.; Xiong, X.; Jiang, Y.; Zou, F.; Hu, X.; Xin, Y.; Zhang, Z.; Huang, Y., Synthesis of Functionalized 3d Hierarchical Porous Carbon for High-Performance Supercapacitors. *Energy Environ. Sci.* **2013,** *6*, 2497-2504.
26. Xie, Q.; Bao, R.; Xie, C.; Zheng, A.; Wu, S.; Zhang, Y.; Zhang, R.; Zhao, P., Core-Shell N-Doped Active Carbon Fiber@Graphene Composites for Aqueous Symmetric Supercapacitors with High-Energy and High-Power Density. *J. Power Sources* **2016,** *317*, 133-142.
27. Yeom, D.-Y.; Jeon, W.; Tu, N. D. K.; Yeo, S. Y.; Lee, S.-S.; Sung, B. J.; Chang, H.; Lim, J. A.; Kim, H., High-Concentration Boron Doping of Graphene Nanoplatelets by Simple Thermal Annealing and Their Supercapacitive Properties. *Sci. Rep.* **2015,** *5*, 9817.
28. Pan, Z.; Liu, M.; Yang, J.; Qiu, Y.; Li, W.; Xu, Y.; Zhang, X.; Zhang, Y., High Electroactive Material Loading on a Carbon Nanotube@3d Graphene Aerogel for High-Performance Flexible All-Solid-State Asymmetric Supercapacitors. *Adv. Funct. Mater.* **2017,** *27*, 1701122-n/a.
29. Fan, Y.-M.; Song, W.-L.; Li, X.; Fan, L.-Z., Assembly of Graphene Aerogels into the 3d Biomass-Derived Carbon Frameworks on Conductive Substrates for Flexible Supercapacitors. *Carbon* **2017,** *111*, 658-666.

30. Fan, Z.; Liu, Y.; Yan, J.; Ning, G.; Wang, Q.; Wei, T.; Zhi, L.; Wei, F., Template-Directed Synthesis of Pillared-Porous Carbon Nanosheet Architectures: High-Performance Electrode Materials for Supercapacitors. *Adv. Energy Mater.* **2012,** *2*, 419-424.
31. Garlof, S.; Mecklenburg, M.; Smazna, D.; Mishra, Y. K.; Adelung, R.; Schulte, K.; Fiedler, B., 3d Carbon Networks and Their Polymer Composites: Fabrication and Electromechanical Investigations of Neat Aerographite and Aerographite-Based Pncs under Compressive Load. *Carbon* **2017,** *111*, 103-112.
32. Peng, H.; Ma, G.; Sun, K.; Mu, J.; Zhang, Z.; Lei, Z., Facile Synthesis of Poly(P-Phenylenediamine)-Derived Three-Dimensional Porous Nitrogen-Doped Carbon Networks for High Performance Supercapacitors. *J. Phys. Chem. C* **2014,** *118*, 29507-29516.
33. Huang, P.; Li, H.; Huang, X.; Chen, D., Multiheteroatom-Doped Porous Carbon Catalyst for Oxygen Reduction Reaction Prepared Using 3d Network of Zif-8/Polymeric Nanofiber as a Facile-Doping Template. *ACS Appl. Mater. Interfaces* **2017,** *9*, 21083-21088.
34. Zhang, X.; Ma, L.; Gan, M.; Fu, G.; Jin, M.; Lei, Y.; Yang, P.; Yan, M., Fabrication of 3d Lawn-Shaped N-Doped Porous Carbon Matrix/Polyaniline Nanocomposite as the Electrode Material for Supercapacitors. *J. Power Sources* **2017,** *340*, 22-31.
35. Chen, L.-F.; Huang, Z.-H.; Liang, H.-W.; Guan, Q.-F.; Yu, S.-H., Bacterial-Cellulose-Derived Carbon Nanofiber@Mno2 and Nitrogen-Doped Carbon Nanofiber Electrode Materials: An Asymmetric Supercapacitor with High Energy and Power Density. *Adv. Mater.* **2013,** *25*, 4746-4752.
36. Kim, B.-H.; Yang, K. S.; Ferraris, J. P., Highly Conductive, Mesoporous Carbon Nanofiber Web as Electrode Material for High-Performance Supercapacitors. *Electrochim. Acta* **2012,** *75*, 325-331.
37. Simon, P.; Gogotsi, Y., Materials for Electrochemical Capacitors. *Nat. Mater.* **2008,** *7*, 845.
38. Liu, J.; Zhang, L.; Wu, H. B.; Lin, J.; Shen, Z.; Lou, X. W., High-Performance Flexible Asymmetric Supercapacitors Based on a New Graphene Foam/Carbon Nanotube Hybrid Film. *Energy Environ. Sci.* **2014,** *7*, 3709-3719.
39. Ma, C.; Sheng, J.; Ma, C.; Wang, R.; Liu, J.; Xie, Z.; Shi, J., High-Performanced Supercapacitor Based Mesoporous Carbon Nanofibers with Oriented Mesopores Parallel to Axial Direction. *Chem. Eng. J.* **2016,** *304*, 587-593.
40. Xie, W.; Jiang, X.; Qin, T.; Yang, H.; Liu, D.; He, D., Inner Porous Carbon Nanofibers as Binder-Free Electrodes for High-Rate Supercapacitors. *Electrochim. Acta* **2017,** *258*, 1064-1071.
41. Ma, C.; Li, Y.; Shi, J.; Song, Y.; Liu, L., High-Performance Supercapacitor Electrodes Based on Porous Flexible Carbon Nanofiber Paper Treated by Surface Chemical Etching. *Chem. Eng. J.* **2014,** *249*, 216-225.
42. Fan, L.; Yang, L.; Ni, X.; Han, J.; Guo, R.; Zhang, C., Nitrogen-Enriched Meso-Macroporous Carbon Fiber Network as a Binder-Free Flexible Electrode for Supercapacitors. *Carbon* **2016,** *107*, 629-637.
43. Chen, L.-F.; Lu, Y.; Yu, L.; Lou, X. W., Designed Formation of Hollow Particle-Based Nitrogen-Doped Carbon Nanofibers for High-Performance Supercapacitors. *Energy Environ. Sci.* **2017,** *10*, 1777-1783.
44. Xue, Y.; Dai, P.; Zhou, M.; Wang, X.; Pakdel, A.; Zhang, C.; Weng, Q.; Takei, T.; Fu, X.; Popov, Z. I.; Sorokin, P. B.; Tang, C.; Shimamura, K.; Bando, Y.; Golberg, D., Multifunctional Superelastic Foam-Like Boron Nitride Nanotubular Cellular-Network Architectures. *ACS Nano* **2017,** *11*, 558-568.

45. Im, J. S.; Jang, J.-S.; Lee, Y.-S., Synthesis and Characterization of Mesoporous Electrospun Carbon Fibers Derived from Silica Template. *J. Ind. Eng. Chem.* **2009,** *15*, 914-918.
46. Cheng, Y.; Huang, L.; Xiao, X.; Yao, B.; Hu, Z.; Li, T.; Liu, K.; Zhou, J., Cross-Linked Carbon Network with Hierarchical Porous Structure for High Performance Solid-State Electrochemical Capacitor. *J. Power Sources* **2016,** *327*, 488-494.
47. Guo, X.; Zhang, X.; Song, H.; Zhou, J., Electrospun Cross-Linked Carbon Nanofiber Films as Free-Standing and Binder-Free Anodes with Superior Rate Performance and Long-Term Cycling Stability for Sodium Ion Storage. *J. Mater. Chem.* **2017,** *5*, 21343-21352.
48. Puthusseri, D.; Aravindan, V.; Anothumakkool, B.; Kurungot, S.; Madhavi, S.; Ogale, S., From Waste Paper Basket to Solid State and Li-Hec Ultracapacitor Electrodes: A Value Added Journey for Shredded Office Paper. *Small* **2014,** *10*, 4395-4402.
49. Luo, W.; Wang, B.; Heron, C. G.; Allen, M. J.; Morre, J.; Maier, C. S.; Stickle, W. F.; Ji, X., Pyrolysis of Cellulose under Ammonia Leads to Nitrogen-Doped Nanoporous Carbon Generated through Methane Formation. *Nano Lett.* **2014,** *14*, 2225-2229.
50. Wang, S.; Zhang, L.; Xia, Z.; Roy, A.; Chang, D. W.; Baek, J.-B.; Dai, L., Bcn Graphene as Efficient Metal-Free Electrocatalyst for the Oxygen Reduction Reaction. *Angew. Chem. Int. Ed.* **2012,** *51*, 4209-4212.
51. Zhou, J.-H.; Sui, Z.-J.; Zhu, J.; Li, P.; Chen, D.; Dai, Y.-C.; Yuan, W.-K., Characterization of Surface Oxygen Complexes on Carbon Nanofibers by Tpd, Xps and Ft-Ir. *Carbon* **2007,** *45*, 785-796.
52. Zhu, S.; Li, J.; Li, Q.; He, C.; Liu, E.; He, F.; Shi, C.; Zhao, N., Space-Confined Synthesis of Three-Dimensional Boron/Nitrogen-Doped Carbon Nanotubes/Carbon Nanosheets Line-in-Wall Hybrids and Their Electrochemical Energy Storage Applications. *Electrochim. Acta* **2016,** *212*, 621-629.
53. Béguin, F.; Presser, V.; Balducci, A.; Frackowiak, E., Carbons and Electrolytes for Advanced Supercapacitors. *Adv. Mater.* **2014,** *26*, 2219-2251.
54. He, Y.; Chen, W.; Li, X.; Zhang, Z.; Fu, J.; Zhao, C.; Xie, E., Freestanding Three-Dimensional Graphene/Mno2 Composite Networks as Ultralight and Flexible Supercapacitor Electrodes. *ACS Nano* **2013,** *7*, 174-182.
55. Hulicova-Jurcakova, D.; Kodama, M.; Shiraishi, S.; Hatori, H.; Zhu, Z. H.; Lu, G. Q., Nitrogen-Enriched Nonporous Carbon Electrodes with Extraordinary Supercapacitance. *Adv. Funct. Mater.* **2009,** *19*, 1800-1809.
56. El-Kady, M. F.; Strong, V.; Dubin, S.; Kaner, R. B., Laser Scribing of High-Performance and Flexible Graphene-Based Electrochemical Capacitors. *Science* **2012,** *335*, 1326-1330.
57. Huang, K.; Yao, Y.; Yang, X.; Chen, Z.; Li, M., Fabrication of Flexible Hierarchical Porous Nitrogen-Doped Carbon Nanofiber Films for Application in Binder-Free Supercapacitors. *Mater. Chem. Phys.* **2016,** *169*, 1-5.
58. Zhang, L.; Jiang, Y.; Wang, L.; Zhang, C.; Liu, S., Hierarchical Porous Carbon Nanofibers as Binder-Free Electrode for High-Performance Supercapacitor. *Electrochim. Acta* **2016,** *196*, 189-196.
59. Weng, Z.; Su, Y.; Wang, D.-W.; Li, F.; Du, J.; Cheng, H.-M., Graphene-Cellulose Paper Flexible Supercapacitors. *Adv. Energy Mater.* **2011,** *1*, 917-922.
60. Yu, D.; Dai, L., Self-Assembled Graphene/Carbon Nanotube Hybrid Films for Supercapacitors. *J. Phys. Chem. Lett.* **2010,** *1*, 467-470.

61. Qin, K.; Kang, J.; Li, J.; Shi, C.; Li, Y.; Qiao, Z.; Zhao, N., Free-Standing Porous Carbon Nanofiber/Ultrathin Graphite Hybrid for Flexible Solid-State Supercapacitors. *ACS Nano* **2015,** *9*, 481-487.
62. Sheng, H.; Wei, M.; D'Aloia, A.; Wu, G., Heteroatom Polymer-Derived 3d High-Surface-Area and Mesoporous Graphene Sheet-Like Carbon for Supercapacitors. *ACS Appl. Mater. Interfaces* **2016,** *8*, 30212-30224.
63. Wang, X.; Liu, B.; Wang, Q.; Song, W.; Hou, X.; Chen, D.; Cheng, Y.-b.; Shen, G., Three-Dimensional Hierarchical Gese2 Nanostructures for High Performance Flexible All-Solid-State Supercapacitors. *Adv. Mater.* **2013,** *25*, 1479-1486.
64. Peng, X.; Liu, H.; Yin, Q.; Wu, J.; Chen, P.; Zhang, G.; Liu, G.; Wu, C.; Xie, Y., A Zwitterionic Gel Electrolyte for Efficient Solid-State Supercapacitors. *Nat. Commun.* **2016,** *7*, 11782.
65. Subramanian, V.; Zhu, H.; Vajtai, R.; Ajayan, P. M.; Wei, B., Hydrothermal Synthesis and Pseudocapacitance Properties of Mno2 Nanostructures. *J. Phys. Chem. B* **2005,** *109*, 20207-20214.
66. Wang, G.; Wang, H.; Lu, X.; Ling, Y.; Yu, M.; Zhai, T.; Tong, Y.; Li, Y., Solid-State Supercapacitor Based on Activated Carbon Cloths Exhibits Excellent Rate Capability. *Adv. Mater.* **2014,** *26*, 2676-2682.
67. Hu, S.; Rajamani, R.; Yu, X., Flexible Solid-State Paper Based Carbon Nanotube Supercapacitor. *Appl. Phys. Lett.* **2012,** *100*, 104103.

Graphical Table of Contents

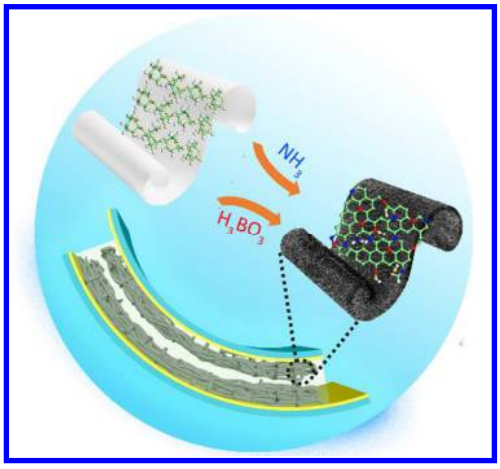

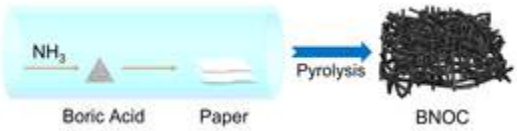

Figure 1 Schematic diagram illustrating the synthetic strategy of BNOCs.

22x6mm (300 x 300 DPI)

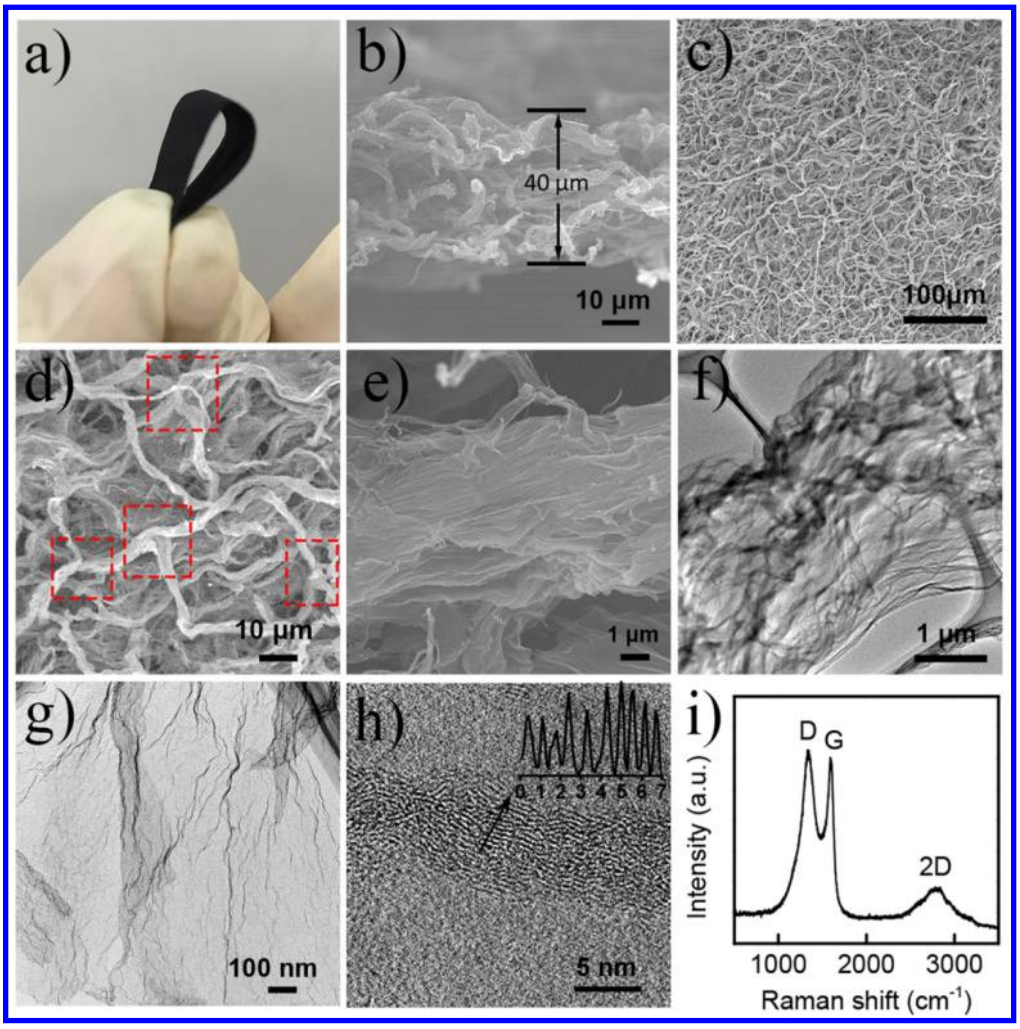

Figure 2 a) Digital image of BNOC-30. b) Side view SEM image of BNOC-30. c), d), e) Top view SEM images of BNOC-30 under different magnifications. f), g), h) TEM images of BNOC-30 at different magnifications. The inset in h) shows the contrast intensity profile recorded along the arrows. i) Raman spectrum of BNOC-30.

140x141mm (300 x 300 DPI)

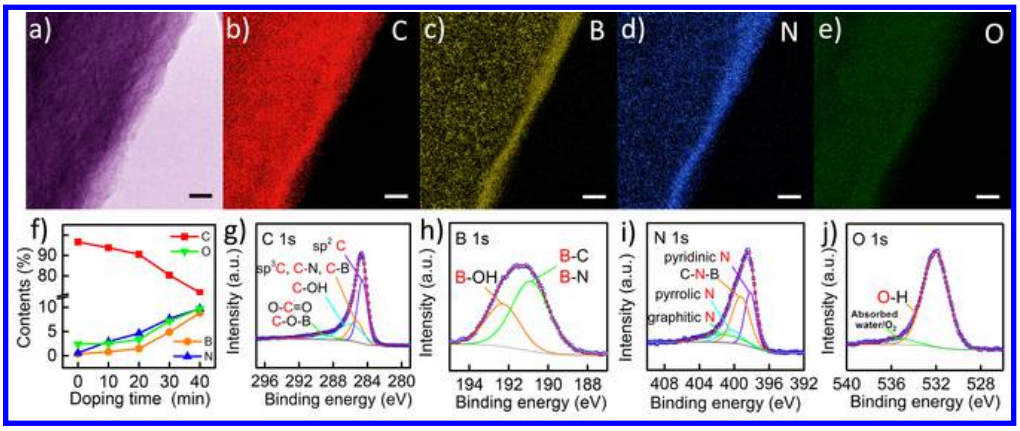

Figure 3 a) Representative energy filtered TEM (EFTEM) image of BNOC-30, scale bar is 20 nm. b-e) EELS elemental maps of C, B, N, O. f) Atomic contents of B, N, O and C at different doping times. g-j) High-resolution C1s spectrum, B 1s spectrum, N 1s spectrum and O 1s spectrum of BNOC-30.

56x23mm (300 x 300 DPI)

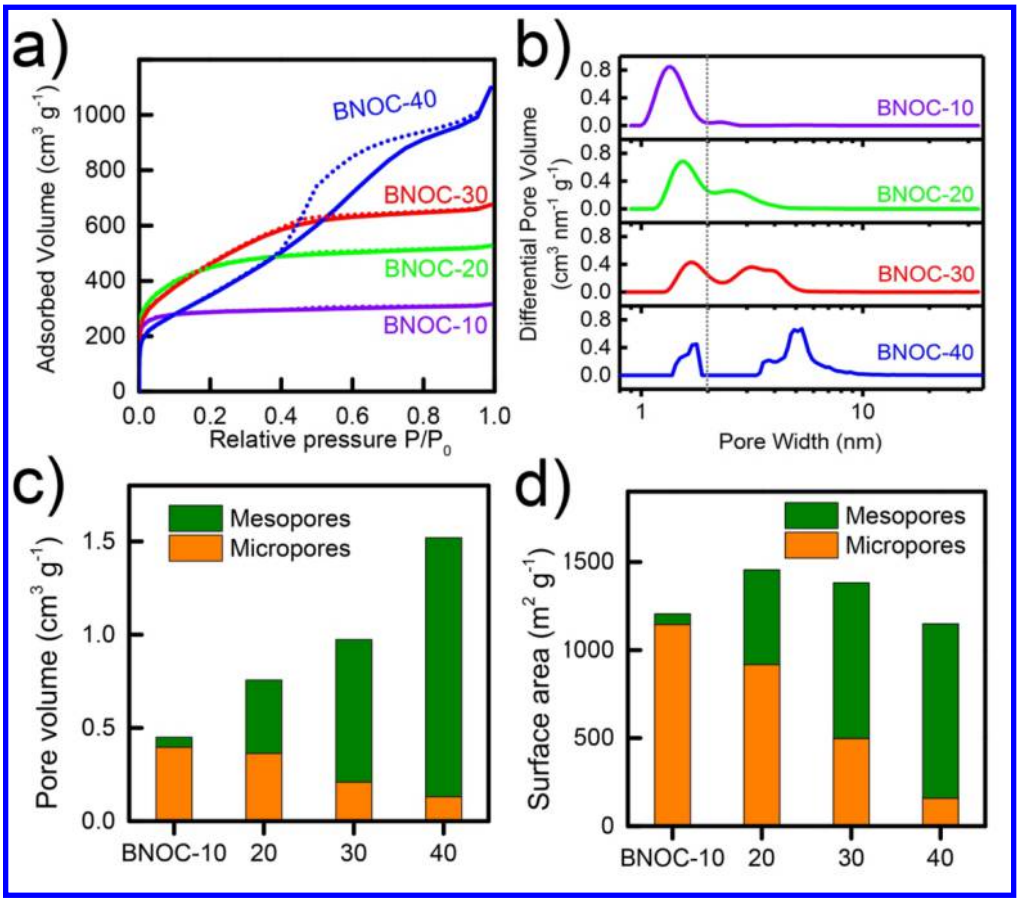

Figure 4 a) Nitrogen adsorption–desorption isotherms of BNOCs. b) Pore size distribution of BNOCs using the quenched solid state functional theory. c), d) Total pore volume and specific surface area comparison of BNOCs.

123x108mm (300 x 300 DPI)

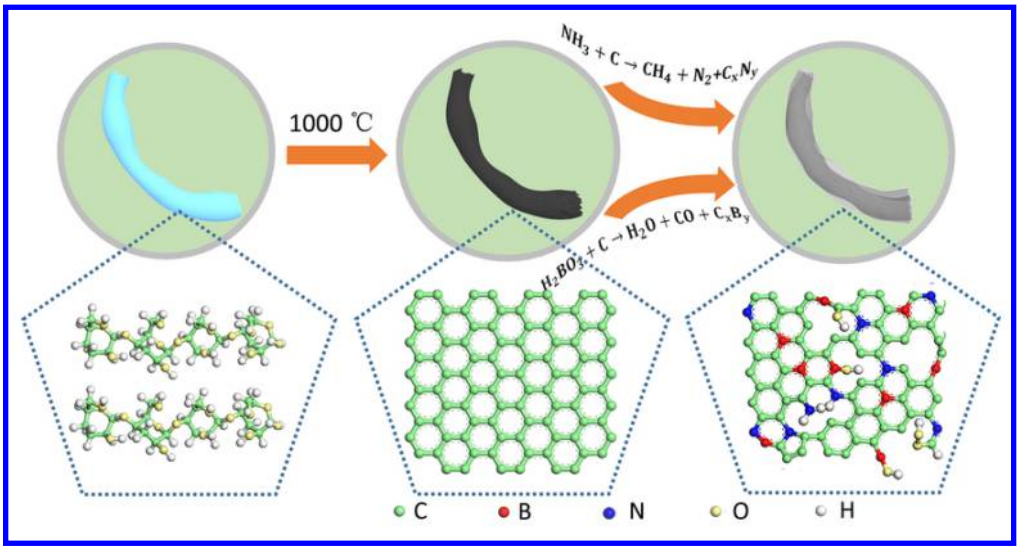

Figure 5 Schematic diagram showing the reaction process under the developed chemical vapor etching & doping strategy.

73x38mm (300 x 300 DPI)

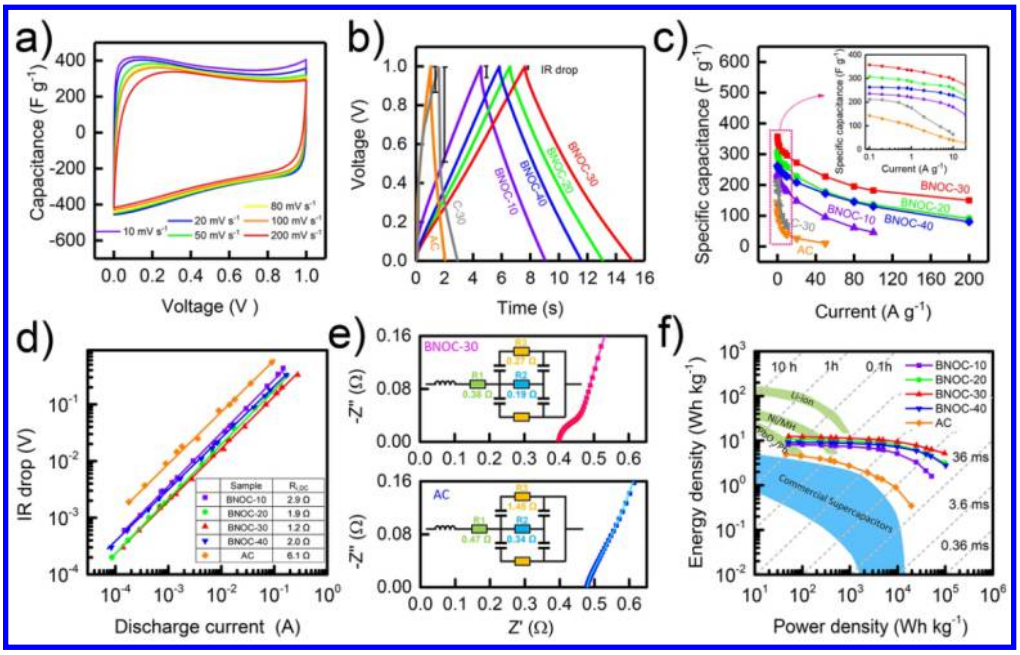

Figure 6 a) CV curves of BNOC-30 at different scan rates. b) GCD profiles of BNOC-10, BNOC-20, BNOC-30, BNOC-40, C-30 and AC at a current density of 10 A g-1. c) Specific capacitance of BNOC-10, BNOC-20, BNOC-30, BNOC-40, C-30 and AC as a function of current densities. The inset shows the magnifying figure of curves in the red frame. d) Initial voltage drops of BNOCs and AC at different galvanostatic discharge currents. e) High frequency regions of the Nyquist plots of BNOC-30 (top) and AC (bottom) and the corresponding equivalent circuits. f) Ragone plots of BNOCs and AC based supercapacitors.

101x64mm (300 x 300 DPI)

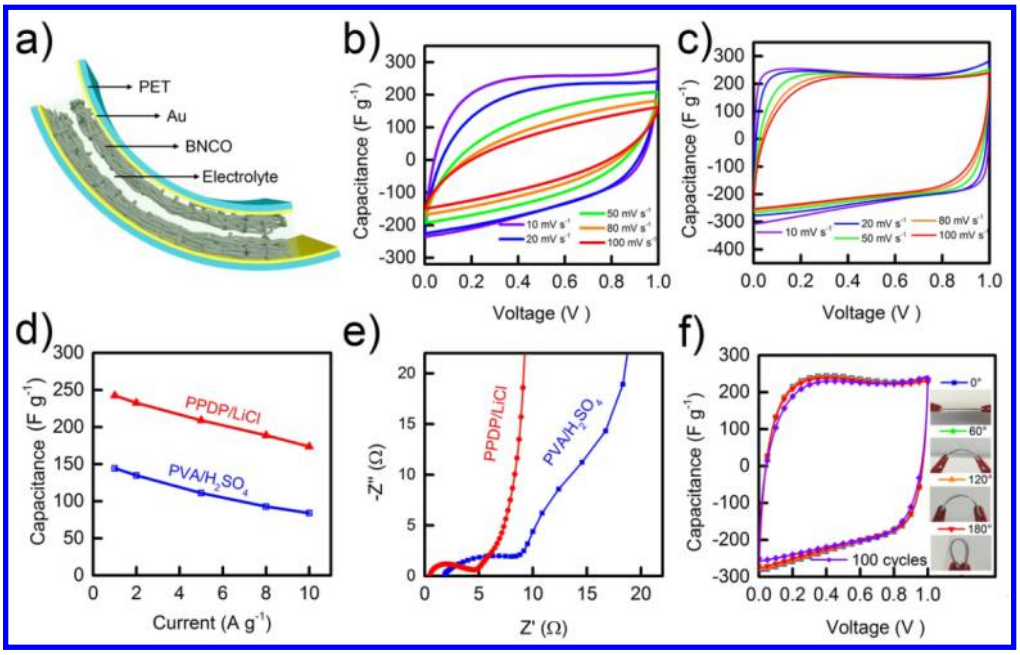

Figure 7 a) Schematics of the stacked ASSS. b) CV curves of ASSS with PVA/H2SO4 electrolyte scanned from 10 mV s-1 to 100 mV s-1. c) CV curves of ASSS with PPDP/LiCl electrolyte scanned from 10 mV s-1 to 100 mV s-1. d) Specific capacitances as a function of current densities. e) Nyquist plots of ASSS with PVA/H2SO4 and PPDP/LiCl electrolyte. f) CV curves at different bending angles with scan rate of 100 mV s-1.

100x63mm (300 x 300 DPI)